ORIGINAL PAPER

Investigating Geophysical Indicators of Permeability Change During Laboratory Hydraulic Shearing of Granitic Fractures with Surface Roughness

Takuya Ishibashi[1] [iD] **· Hiroshi Asanuma[1]**

Abstract

In order to investigate geophysical indicators of permeability changes in subsurface fractures, we conducted an experimental study on the hydraulic–mechanical–seismic coupled behaviors of granite fractures with surface roughness under stress conditions during hydraulic shearing. Our laboratory experiment yielded the following insights: (1) The "self-propping shear slip concept" unequivocally serves as the primary mechanism for maintaining the increase in fracture permeability of granite, even under stress conditions exceeding approximately 50 MPa. (2) The Gutenberg–Richter b-value gradually decreases during shear dilation and accompanying increase in fracture permeability. Thus, it could serve as an indicator for assessing changes in fracture permeability. (3) The evolution amplitude in acoustic emissions (AEs), as well as the classification of tensile/shear modes and the timing of our maximum amplitude of AE occurrence, do not seem to provide useful information for estimating fracture permeability changes during hydraulic shear slip. The reduction in b-value can be attributed to the spontaneous formation of preferential flow paths during the injection of pressurized fluid into the rock fracture and the subsequent detachment of the small contacting asperities due to localized shear slips, which naturally lead to the creation of porosity and irreversible increase in fracture permeability.

Highlights

- Hydraulic-mechanical-seismic coupled behaviors of granitic fracture are investigated during hydraulic shearing experiments in the laboratory.
- b-value gradually decreases during shear dilation and associated permeability increase of granitic fracture with rough surfaces.
- There is no clear correlation between fracture permeability change and amplitude/occurrence timing of $AE_{max\ amp}$. during hydraulic shearing.

✉ Takuya Ishibashi
   takuya.ishibashi@aist.go.jp

   Hiroshi Asanuma
   h.asanuma@aist.go.jp

[1] Fukushima Renewable Energy Institute, National Institute of Advanced Industrial Science and Technology, 2-2-9, Machiike-dai, Koriyama, Fukushima 963-0298, Japan

1 Introduction

In subsurface energy extraction from geothermal or oil/gas reservoirs, various human operations, including the injection of pressurized fluids into the reservoirs, are crucial for enhancing or maintaining the hydraulic performance of subsurface rock fractures. A key research topic during such operations, not to mention the theme of mitigating seismicity (Ellsworth 2013; Ge & Saar 2022; Zang et al. 2014), is quantifying the spatio-temporal changes in subsurface permeability structure within rock fractures, preferably in real-time or quasi-real-time. While well testing directly confirms the subsurface hydraulic properties of fractures, improving the accuracy of estimation necessitates drilling multiple wells for continuous monitoring of fluid pressure, flow rate, temperature, and other parameters. However, due to the high costs associated with well drilling and subsequent testing (U.S. Department of energy 2019), the number of wells drilled to estimate subsurface permeability is usually limited. Therefore, it is desirable to investigate and establish methods for indirectly estimating and monitoring the spatio-temporal changes in subsurface permeability structure within rock fractures, even with a limited number of monitoring wells.

For instance, during pressurized fluid injection into subsurface rock fractures at intermediate to field scales, geophysical data such as microseismic events, seismic tomography, and electrical surveys are monitored and recorded alongside the injection history (e.g., wellhead pressure and flow rate) (Fu et al. 2021; Johnson et al. 2021; Schoenball et al. 2020). These geophysical explorations are generally more cost-effective compared to well-based observations. While it is widely acknowledged that these geophysical data can serve as valuable indicators for studying active subsurface processes (e.g., fracture opening/closure, shear slip, and coalescence) or the three-dimensional spatial distribution of crustal fluids within subsurface fracture system, few efforts have been made to quantitatively link the obtained geophysical parameters to the hydraulic properties of subsurface fractures based on the physical processes occurring within them (Fang et al. 2018; Ishibashi et al. 2016). This situation primarily arises from the fact that multiple rock fractures are typically distributed in a three-dimensional network in the subsurface (Berkowitz et al. 2000; Bonnet et al. 2001), making it extremely challenging to interpret the coupled hydraulic and geophysical behaviors within a specific area of interest. Conversely, conducting hydraulic–mechanical coupled experiments in a laboratory setting, where the stress states and boundary conditions can be accurately controlled (e.g., Ishibashi et al. 2023), plays a crucial role in establishing a quantitative connection between hydraulic properties and geophysical parameters.

Therefore, as an initial step toward indirectly estimating the spatio-temporal changes in subsurface hydraulic properties within rock fractures, we investigate the existence of a quantitative correlation between hydraulic and geophysical properties for a single granitic fracture based on a novel hydraulic-mechanical coupled experiment conducted in the laboratory. During these experiments, the rock fracture undergoes a cycle of opening, hydraulic shear slip, and closure, which repeats three times in sequence. Simultaneously, we record acoustic emission data, providing an opportunity to examine the micromechanical processes associated with the interactive changes in hydraulic and geophysical properties of rock fractures.

2 Experimental Methods

We conduct laboratory hydraulic shear experiments on a granitic rock fracture to investigate geophysical indicators of permeability changes under stress. During the experiments, acoustic emission (AE) data are continuously recorded and synchronized with the mechanical and hydraulic responses of the rock fracture. A portion of experimental results (i.e., temporal evolutions of pressures and fracture permeability during hydraulic shear slips) has been reported in Ishibashi et al. (2023), but the comprehensive analysis of AE data was omitted due to reservation pertaining to the quality of the AE data.

2.1 Rock Fracture and Surface Profiling

For laboratory experiments, we select Inada granite sampled from Ibaraki, Japan, as its fundamental physical properties have been well investigated (Fujii et al. 2005; Lin et al. 1995, 2003; Oda et al. 2002; Takahashi et al. 1990). Inada granite composed of quartz (36 wt%), alkaline feldspar (28 wt%), plagioclase (32 wt%), and biotite (4 wt%), has a mean grain size of approximately 2 mm. The physical properties of Inada granite are summarized in Table 1. We prepare a cylindrical granite sample (50 mm in diameter and 100 mm in length) with a single tensile fracture in the shape of an ellipse (major axis: 70.7 mm, minor axis: 50 mm) (Fig. 1a). The fracture plane is tilted precisely 45-degrees angle from the long axis of the cylindrical sample, dividing it into two blocks (footwall side and hanging wall side). Each block has a single borehole (diameter ~ 2 mm) for fluid injection or drainage. Before the experiments, the cylindrical sample is dried in an oven at a temperature of 80 ℃ for 24 h.

The surface topographies of the footwall and hanging wall are measured using a 3-D measuring microscope (Keyence, VR-3050) with a vertical resolution of 0.5 μm and a horizontal resolution of 23.4 μm (Fig. 1a). Fractal dimension (D) is calculated using the spectral method (Fig. 1b)

Table 1 Fundamental physical properties of Inada granite

Properties	Value	References
Density (kg/m^3)	2630 (Dry), 2640 (Wet)	Lin et al. (2003)
Porosity (%)	0.45~0.6	Oda et al. (2002); Lin et al. (1995); Takahashi et al. (1990)
Young's modulus (GPa)	63 (H), 65 (G), 68 (R)	Oda et al. (2002); Lin et al. (2003)
Poisson's ratio	0.33 (H), 0.25 (G), 0.28 (R)	Oda et al. (2002)
UCS (MPa)	167 (H), 188 (G), 196 (R)	Oda et al. (2002)
P-wave velocity (km/s)	4.73 (H), 4.36 (G), 4.16 (R)	Oda et al. (2002); Lin et al. (2003)
S-wave velocity (km/s)	2.74 (H), 2.44 (G), 2.52 (R)	Oda et al. (2002); Lin et al. (2003)
Tensile strength (MPa)	7.9 (H), 7.1 (G), 4.3 (R)	Fujii et al. (2005); Lin et al. (2003)
Matrix permeability (m^2)	2E-20~5E-19	Takahashi et al. (1990)

Note that (H), (G), (R) represent Hardway plane, Grain plane, and Rift plane, respectively
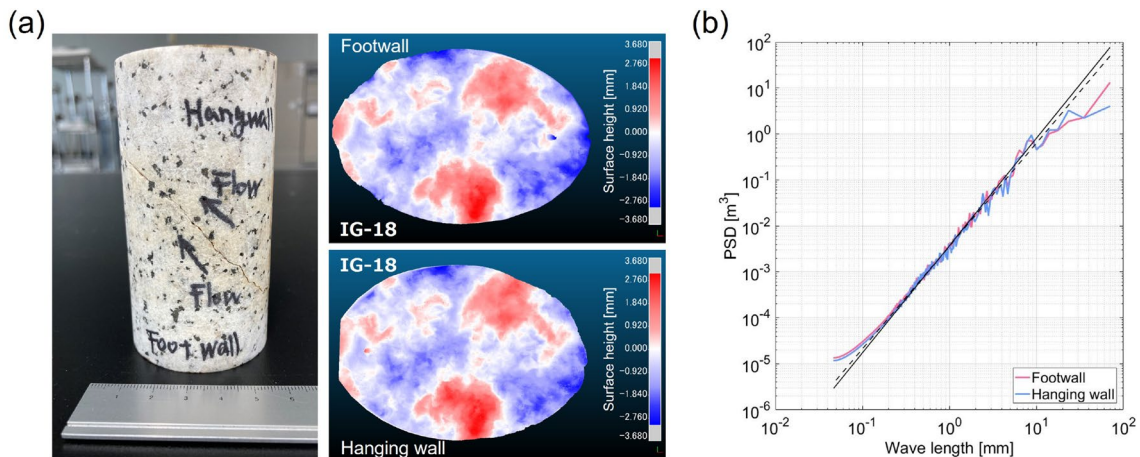

Fig. 1 **a** A cylindrical granite specimen containing a single tensile fracture with an elliptical shape (IG-18) and corresponding surface topographies of the footwall and hanging wall. **b** The relationship between power spectral density and wavelength for IG-18

(Brown & Scholz 1985; Matsuki et al. 2006; Power et al. 1987), and the joint roughness coefficient (*JRC*) is estimated using the empirical relation reported in Yu and Vayssade (1991). It should be noted that *D* and *JRC* are evaluated based on the 2-D line profiles in the direction of the elliptical fracture's major axis, and the values are averaged across all line profiles. The calculated *D* values for Inada granite fracture are 1.33 (footwall) and 1.38 (hanging wall), while the *JRC* values are 15.3 (footwall) and 13.9 (hanging wall). According to the *JRC* values, the fracture surfaces used in this study can be classified as "very rough" fractures (Barton & Choubey 1977).

2.2 Experimental Apparatus and Experimental Procedure

We perform hydraulic shear experiments using a triaxial apparatus (Fig. 2), in which the confining pressure (P_{conf}) and pore fluid pressure (both inlet and outlet sides, P_{in} and P_{out}) are independently controlled by three syringe pumps

(TELEDYNE ISCO 260D for confining pressure and two TELEDYNE ISCO 500D for pore fluid pressure). These syringe pumps have a pressure error of $\pm 0.5\%$. Silicone oil is used as the pressure medium for confining stress, while distilled water serves as the flowing fluid. The cylindrical rock sample is placed between cylindrical metal pistons and enclosed in triple thermal shrinkable tubes (Teflon + silicone + polyolefin) to isolate the sample and internal fluid pressure from the confining fluid. The axial force is measured inside the pressure vessel using an internal load cell and electrically servocontrolled with an accuracy of 0.1 kN. The axial displacement of the rock sample is measured using a linear variable differential transformer (LVDT) mounted inside the pressure vessel. The accuracy of the axial displacement measurement is 0.1 μm with an associated error of $\pm 0.5\%$. Throughout the experiments, pressure, flow rate, and the evolving volume of three syringe pumps (Pump A, B, and C in Fig. 2b), axial stress, and axial displacement (11 parameters in total) are continuously monitored and recorded at a sampling rate of 100 Hz.
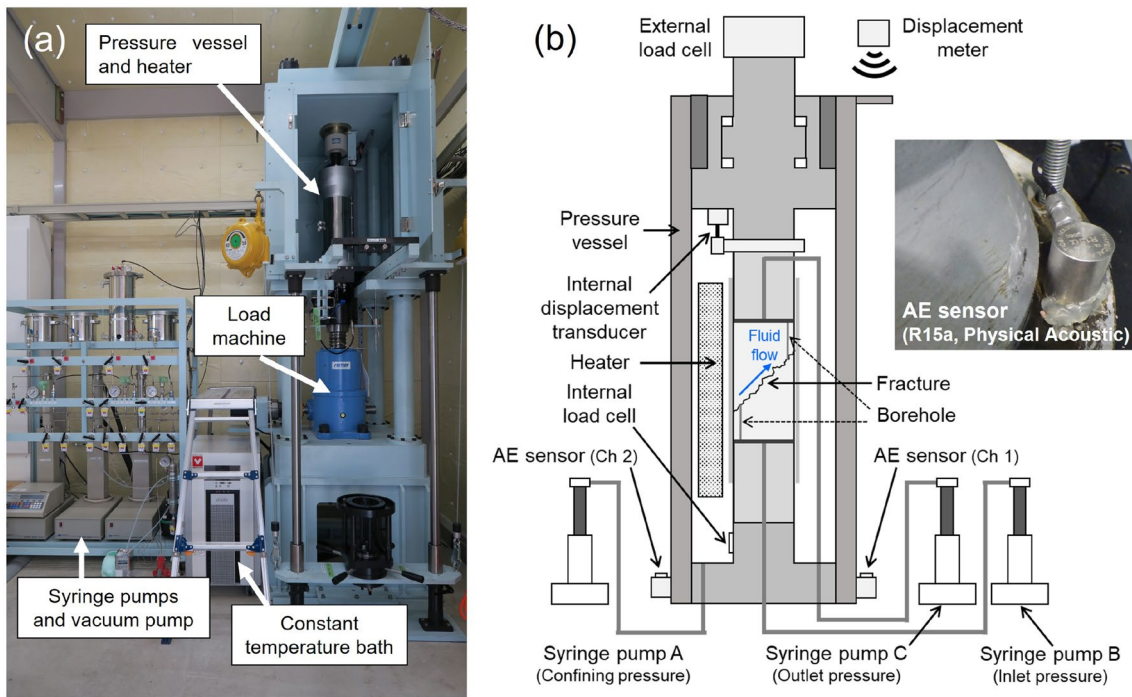
Fig. 2 a The experimental system used for the hydraulic shearing experiment. This system was installed at Fukushima Renewable Energy Institute, AIST, in 2016. **b** The experimental arrangement designed to measure the hydromechanical parameters of the rock fracture during hydraulic shearing

We also record acoustic emissions using two independent AE sensors (Physical Acoustic Corp., R15a) with a diameter of 19 mm and a resonant frequency of 150 kHz. These sensors are attached outside of the pressure vessel (Fig. 2b) using glue. The PCI-2 system (Physical Acoustic Corp.) with 18-bit A/D and 40 MS/s acquisition is combined with AEwin™ software (Physical Acoustic Corp.) for processing the AE data. During the experiments, event counting method, which counts a single AE signal as one (Ohtsu 1996), employed. The signals captured by the AE sensors (Ch 1 and Ch 2) are amplified by 40 dB using preamplifier (Physical Acoustic Corp., 2/4/6) and are then subjected to a 0.02–3.00 MHz band-pass filter. AE signals exceeding the threshold level of 50 dB are recorded at a sampling rate of 10 MS/s. This threshold level is chosen to avoid recording AE signals caused by the servocontrolled motor operation of the load machine. The recorded AE data are synchronized with the aforementioned 11 parameters. Due to the limited number of AE sensors, hypocenter locations of AE events cannot be determined in this study.

In our experimental setup, the confining pressure and axial pressure correspond to the minimum principal compressive stresses (σ_3) and the maximum principal compressive stresses (σ_1) for the cylindrical sample, respectively. Therefore, the normal stress (σ_n) and shear stress (τ) on the fracture plane are calculated by (Cornet 2015; Jaeger et al. 2007)

$$\sigma_n = \sigma_3 + (\sigma_1 - \sigma_3)\sin^2\theta \tag{1}$$

$$\tau = (\sigma_1 - \sigma_3)\sin\theta\cos\theta, \tag{2}$$

where θ is the angle between the σ_3 vector and the normal vector of the fracture plane (constant value of 45 degrees). In the cases of fluid flow and hydraulic shear tests, the pore pressure (P_{pore}) is calculated as the mean value of the inlet fluid pressure and outlet fluid pressure:

$$P_{pore} = \frac{P_{in} + P_{out}}{2}. \tag{3}$$

Since the pore pressure acts against the normal stress on the fracture plane, the effective normal stress (σ_{eff}) is calculated as follows:

$$\sigma_{eff} = \sigma_n - P_{pore}. \tag{4}$$

Hydraulic shearing is triggered when the following criteria is met:

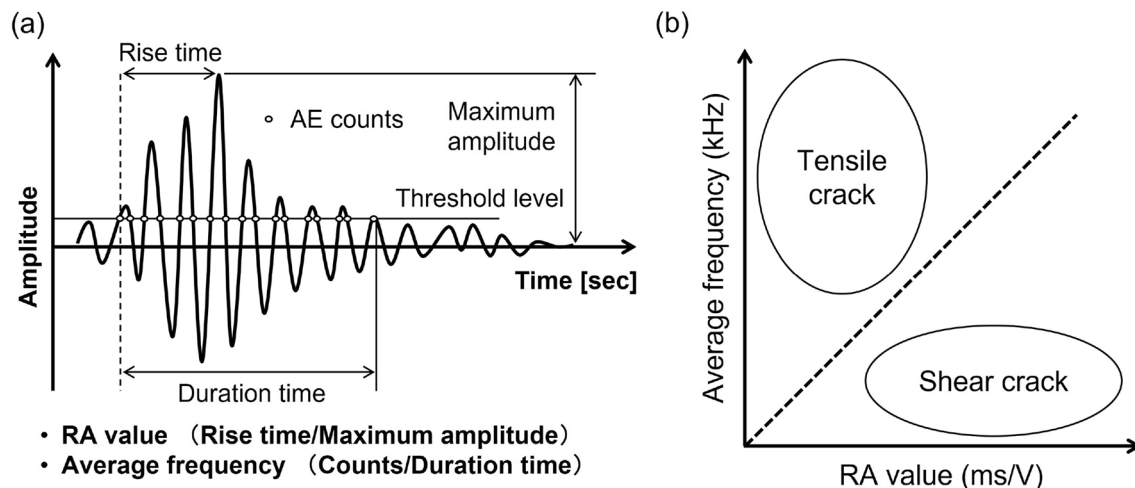$$\tau > C + \mu\sigma_{eff}, \tag{5}$$

Fig. 3 **a** Acoustic Emission (AE) parameters in an AE hit (modified from Ohno and Ohtsu 2010). **b** Relationship between average frequency and RA value for crack mode classification

where C represents the cohesive strength (MPa) and μ is the friction coefficient. The shear slip displacement along the fracture plane (d_{slip}) is approximated by the equation:

$$d_{slip} = \Delta z \cos\theta, \tag{6}$$

where Δz is the axial displacement of the cylindrical rock sample (m), which is caused by hydraulic shearing and is measured inside the pressure vessel. It should be noted that the approximation of the shear slip displacement in Eq. (6) somewhat underestimate the actual value, as it does not consider the shear slip displacement corresponding to the lateral deformation of cylindrical rock sample. On the other hand, the permeability (k) of the rock fractures is evaluated based on the cubic law (Jaeger et al. 2007; Witherspoon et al. 1980):

$$k = \frac{e_h^2}{12}, \tag{7}$$

where e_h represents the hydraulic aperture (m). Assuming that fluid flow occurs only within the fracture plane, the hydraulic aperture can be represented as:

$$e_h = \left(-\frac{12\eta LQ}{w(P_{in} - P_{out})} \right)^{1/3}, \tag{8}$$

where Q is the flow rate at steady state (m³/s), P_{in}-P_{out} (ΔP) is the differential pressure, and η is the fluid viscosity (1.002×10^{-3} Pa·sec at 20 ℃ for distilled water). L and W represent the flow path length (5.05×10^{-2} m) and flow path width (3.4×10^{-2} m), respectively. It is important to note that the estimated fracture permeability is valid when the direction of fluid flow is parallel to the direction of shear slip.

In addition to the number of AE events recorded during the experiment, we analyze the representative AE parameters-Maximum amplitude, RA value, and average frequency-for each AE event (Feng et al. 2019; Ohno and Ohtsu 2010). Figure 3a provides a graphical explanation of how these AE parameters are evaluated based on a typical waveform of AE. The time elapsed from the arrival of AE to the time of maximum amplitude is referred to as the "rise time", while the RA value and average frequency are defined as the ratio of the rise time to the maximum amplitude (sec/V) and the ratio of the ringdown count number to the AE duration time (1/s), respectively. AEwin™ software is used to calculate RA value and average frequency, which are utilized for crack mode classification (tensile type or shear type) as suggested by Ohno and Ohtsu (2010) (Fig. 3b). In Fig. 3b, the threshold line classifying tensile and shear cracks cannot be determined uniquely and requires selection through trial and error.

The experiments are conducted at room temperature (~20 ℃). The confining pressure (σ_3) is set to 8 MPa and maintained constant throughout the experiment using syringe pump A (Fig. 2b). To saturate the fracture plane with distilled water, both the inlet fluid pressure (P_{in}) and outlet fluid pressure (P_{out}) are increased to 0.5 MPa, with P_{out} being kept constant throughout the experiment using syringe pump C (Fig. 2b). Initially, we perform fluid-flow-through experiments at steady state under different axial pressure conditions (σ_1). σ_1 is increased to the target values of 30, 60, 90, 110, and 125 MPa, and these stresses are maintained constant during each stage through electric servocontrol. In each stage, P_{in} is varied between 1.0 and 4.5 MPa (i.e., 0.5 MPa $\leq \Delta P < 4$ MPa) to evaluate the stress dependency of permeability for the non-sheared fracture.

Subsequently, we conduct hydraulic shearing experiments with reference to the method reported in Ye and Ghassemi (2018). At the onset of these experiments, we simulate the critically stressed level of the fracture plane, setting σ_1, σ_3, P_{in}, and P_{out} to 125, 8, 4, and 0.5 MPa, respectively, and controlling all values through servocontrol. Then, the servocontrol of σ_1 is released, and the experimental condition is shifted from constant σ_1 to constant piston displacement, with the bottom position of the pressure vessel locked. This shift in the experimental condition allows for the relaxation of shear stress on the fracture plane during hydraulic shearing, thereby mitigating non-self-arrested large slips on the fracture plane. Once this situation is achieved, we switch the control mode of syringe pump B for P_{in} (Fig. 2b) from constant pressure mode to constant flow rate mode. The injection flow rates are set to 1.5, 2.0, or 3.0 cm³/min, depending on the number of shear slips the target fracture plane has experienced beforehand. Fluid injection continues under drainage conditions until hydraulic shearing is triggered and subsequently self-arrested. The total volume of injected fluid (ΔV_{inj}) during this period is calculated by

$$\Delta V_{inj} = -\Delta V_{B,rem} - \Delta V_{C,rem}, \tag{9}$$

where $\Delta V_{B,rem}$ and $\Delta V_{C,rem}$ are the change in the remaining volumes (m³) of syringe pump B (negative value due to outflow) and syringe pump C (positive value due to inflow). On the other hand, the change in the remaining volumes of syringe pump A ($\Delta V_{A,rem}$) closely corresponds to the change in aperture (or pore space) volume within the fracture (Ishibashi et al. 2020), resulting from the combined effects of elasticity (i.e., normal opening/closure) and plasticity (i.e., shear dilation/compaction). After the completion of the pressurized water injection stage, we switch the control mode of syringe pump B back to constant pressure mode from constant flow rate mode, gradually reducing P_{in} to 3.5 MPa. Once the decompression of P_{in} is completed, σ_1 is restored to the target level of 125 MPa, and the hydraulic shear experiment is repeated in the same manner as described above.

3 Experimental Results

3.1 Temporal Changes in Hydromechanical Parameters, Accumulated Numbers of AEs, and Maximum Amplitude of AEs During Hydraulic Shearing of Granite Fracture

In Fig. 4a, solid square symbols represent the combination of normal stress and shear stress acting on the fracture plane during the fluid-flow-through experiments at steady state. By increasing the axial pressure (σ_1), the normal
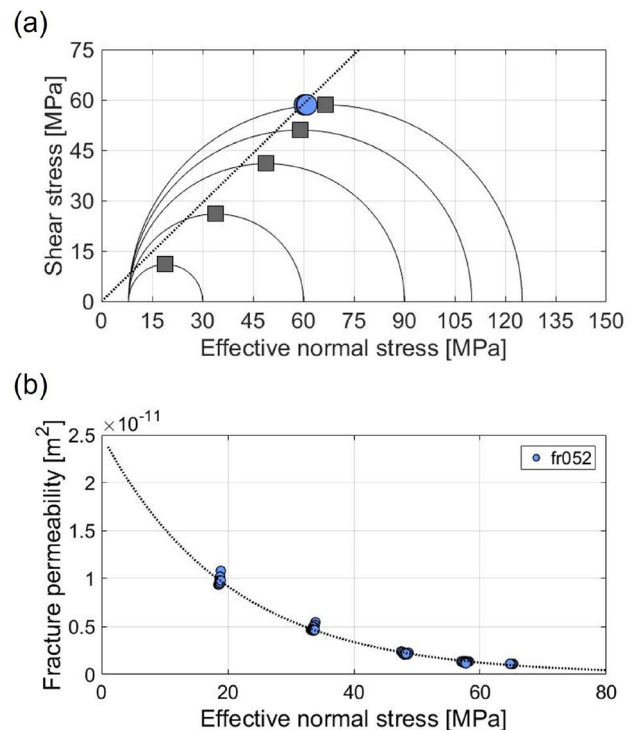
(a)

(b)

Fig. 4 **a** Combination of normal stress and shear stress exerted on the fracture plane during the fluid-flow-through experiments at steady state (Grey squares). Stress states at the onset of hydraulic shear slip are represented by blue circles, and the approximated failure criteria is shown by a dotted line. **b** Relationship between fracture permeability and effective normal stress. Approximated curve by Eq. (10) is also shown

stress is increased to the target values of 19, 34, 49, 59, and 66.5 MPa. The stress dependency of fracture permeability (k) is illustrated in Fig. 4b. Fracture permeability is approximated using the equation (Meng et al. 2022):

$$k = k_0 \exp\left(-\alpha \sigma_{eff}\right), \tag{10}$$

where k_0 is the preexponential factor (m²) corresponding to the fracture permeability under non-loading conditions (i.e., $\sigma_{eff} = 0$) and α is the fitted compressibility coefficient (1/MPa). The values of k_0 and α are 2.5×10^{-11} and 5.0×10^{-2}, respectively.

Figure 5 presents the results of the hydraulic shear experiment, providing a detailed depiction of the temporal changes in raw data, encompassing a total of 10 hydromechanical parameters excluding axial displacement. The inlet fluid pressure (pump B) consistently remains lower than the confining pressure (pump A) to prevent fluid short-circuiting outside the fracture plane (Fig. 5b). During the experiments, we successfully identified three instances of hydraulic shearing (Slip #1, #2, and #3 in Fig. 5) through simultaneous observations of: (1) reduction in axial pressure (Fig. 5a),
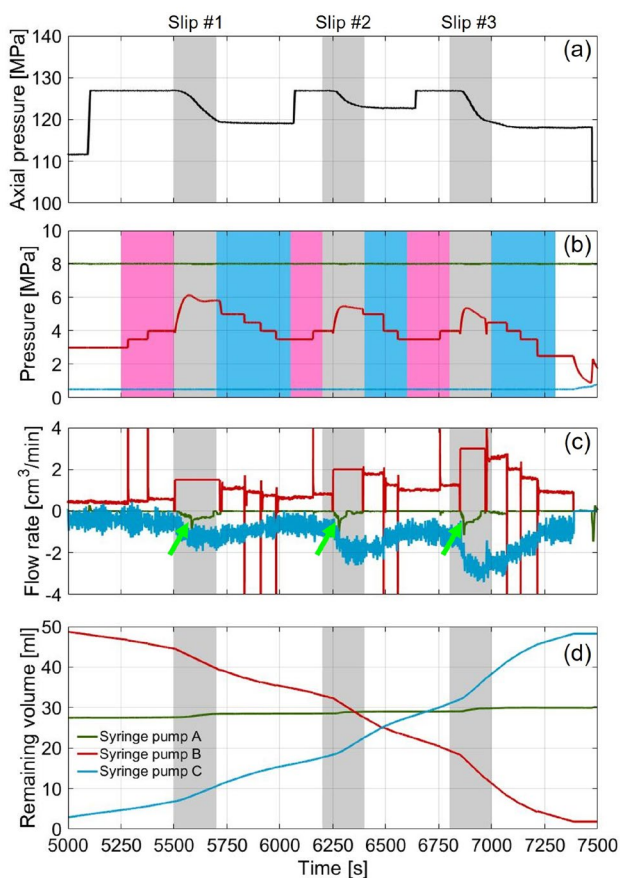
Fig. 5 Results of hydraulic shear experiments. Time-dependent changes in (**a**) axial pressure, (**b**) fluid pressure of pumps, (**c**) flow rate of pumps, and (**d**) remaining volume of pumps. Note that syringe pumps A, B, and C control the flow behaviors of confining fluid, inlet fluid, and outlet fluid, respectively. The pink and blue hatched areas correspond to normal opening and normal closure of the rock fracture, respectively. The green arrows indicate the backflow at syringe pump A, providing evidence of shear-induced dilation of the fracture

(2) decrease in fluid pressure of syringe pump B (Fig. 5b), and (3) backflow at syringe pump A (indicated by green arrows in Fig. 5c). The injection flow rate increases with each shear slip experienced (Fig. 5c), and the total volume of injected fluid can be calculated using Eq. (9) (Fig. 5d). In Fig. 5b, the pink and blue hatched areas, located within the grey area corresponding to the shear slips, represent normal opening and normal closure of the rock fracture, respectively. The solid circles in Fig. 4a denote the combination of normal stress and shear stress acting on the fracture plane when the injection fluid pressure reaches its maximum (i.e., failure criteria for hydraulic shearing). Assuming zero cohesive strength ($C=0$), the apparent friction coefficient (μ') is evaluated to be 0.964.

Figure 6 (Top) illustrates the temporal changes in the accumulated numbers and maximum amplitude of recorded AEs, obtained from independent AE sensors of Channel 1

and Channel 2. Over the analysis period of 2500 s, Channel 1 records a total of 1539 AE events, while Channel 2 records a total of 1122 AE events. The maximum AE amplitudes, amplified by a factor of 100 (equivalent to 40 dB), fall within the range of 50–90 dB. The discrepancy in the total number of AE events primarily arises from the challenge of precisely aligning the sensitivity between AE sensors and the asymmetric positioning of the AE sensors and hypocenters of AEs. On the other hands, the data recorded by the two independent AE sensors share a common characteristic, namely that the cumulative numbers of AEs increase significantly during each hydraulic shear slip and that remain nearly constant during normal opening or normal closure of rock fractures. Furthermore, these data also reveal that the occurrence timing of AEs with large amplitudes is approximately consistent. The relationships between event frequency and maximum amplitudes of AE (A_{max} (mV)) are shown in Fig. 6 (Bottom). The relationship between A_{max} and the maximum amplitude of AE in decibels (A_{dB}) is established by

$$A_{dB} = 10log_{10}A_{max}^2 = 20log_{10}A_{max}, \tag{11}$$

where it should be noted that the recorded amplitudes of AE are pre-amplified by a factor of 100. In Fig. 6 (Bottom), the frequency distributions based on AE amplitude size are depicted in a green histogram, with the number of bins set to 30, and the cumulative numbers of AE events are represented by black solid circles. Figure 6 (Bottom) allows us to recognize that the amplitude distributions of AE events can be described by the Gutenberg–Richter relation (Cornet 2015; Scholz 2002):

$$log_{10}N = a - blog_{10}A_{max}, \tag{12}$$

where N represents the cumulative numbers of AE events with maximum amplitude less than or equal to A_{max} (mV), and a and b are scaling factors. Particularly, b is commonly referred to as the Gutenberg–Richter b-value. A low b-value indicates a relatively high number of larger AEs, and vice versa. In calculating b-value, AE data of both tensile- and shear-type events are normally considered, and the analysis is not restricted to shear-type events only. In this study, the b-value of laboratory AEs is estimated using the maximum likelihood method (Bolton et al. 2021; Utsu 1999):

$$b = \frac{log_{10}e}{(log_{10}A_{max})_{mean} - (log_{10}A_{max})_{min}}, \tag{13}$$

where the subscripts "mean" and "min" denote the average and minimum values, respectively. Furthermore, following the approach of Shi and Bolt (1982), the standard error of the b-value ($\sigma(b)$) can be evaluated as

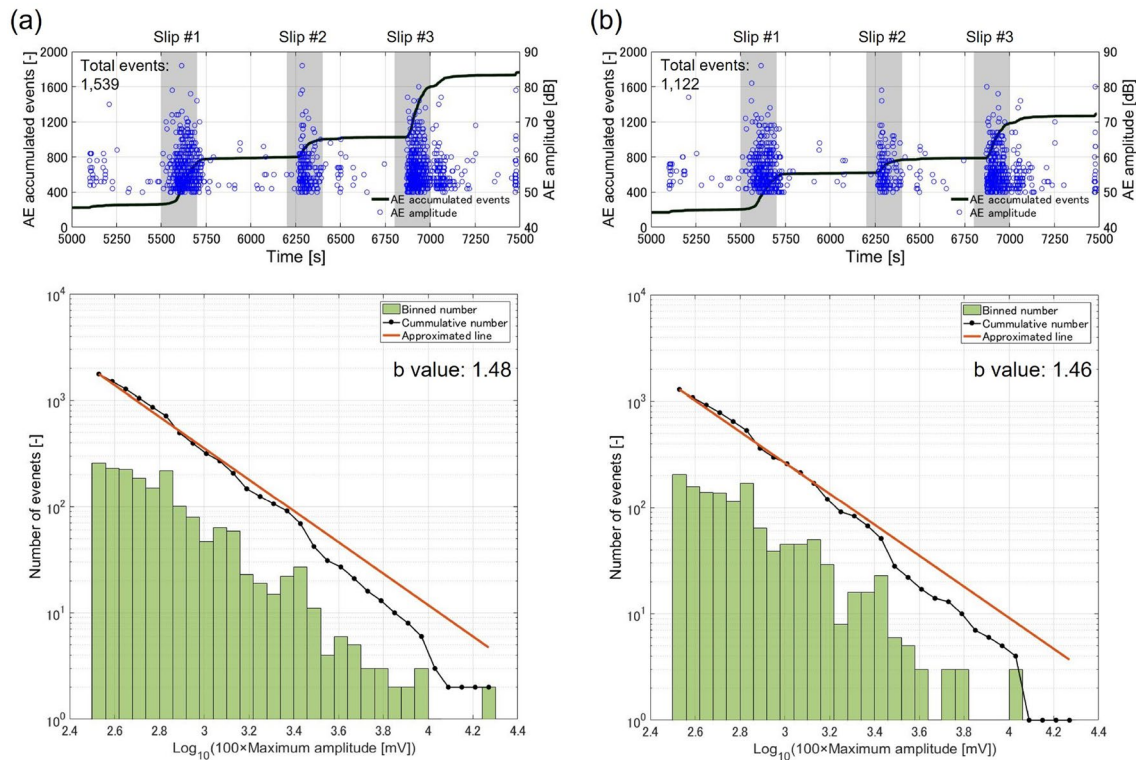$$\sigma(b) = 2.30b^2\sigma(log_{10}A_{max}). \tag{14}$$

Fig. 6 (Top) Time-dependent changes in the accumulated numbers and maximum amplitude of acoustic emissions and (Bottom) the relationship between event frequency and maximum amplitude of acoustic emissions. The Gutenberg–Richter *b*-values are calculated using the maximum likelihood method. **a**, **b** correspond to the data collected by independent acoustic emission sensors, Channel 1 and Channel 2, respectively

$\sigma(log_{10}A_{max})$ is calculated by

$$\sigma^2\left(log_{10}A_{max}\right) = \frac{1}{n-1}\frac{\sum_{i=1}^{n}\left(log_{10}A_{max}^{i} - (log_{10}A_{max})_{mean}\right)^2}{n},$$
(15)

where *n* represents the total number of AE events to be analyzed. With these in mind, the amplitude distributions of AE events are approximated by the Gutenberg–Richter relation, and the approximated results are presented as orange lines in Fig. 6 (Bottom). The calculated *b*-values form the data recorded by the two independent AE sensors (Channel 1 and Channel 2) are 1.48 ± 0.03 and 1.46 ± 0.03, respectively. Considering the consistency of both amplitude distributions of AE events (i.e., histogram) and the calculated *b*-values, we conclude that a series of AE parameters for each AE event are adequately recorded in this study.

3.2 Classification of Failure Modes (Tensile or SHEAR) and Time-Dependent Change in *b*-Value During Hydraulic Shearing of Granite Fractures

For all AE events recorded by the two independent AE sensors during the experiment, the rise angle (sec/V) and the average frequency (1/s) are evaluated using AEwin™ software and plotted in Fig. 7 (Left). According to Ohno and Ohtsu (2010), we can classify the failure mode of each AE, whether tensile or shear, based on the ratio of the rise angle and the average frequency, denoted as *C* (Hz·V/sec). If a given AE event has a higher *C* value than the threshold C_{th}, it is classified as a tensile-type event, whereas an AE event with a lower *C* value than C_{th} is classified as a shear-type event. The threshold C_{th} can vary depending on the rock types and their internal microstructure. Instead of determining a unique C_{th}, we varied C_{th} from 100 (kHz·V/sec), 200 (kHz·V/sec), to 300 (kHz·V/sec). Although the proportion of shear-type AE events slightly increases with an increase in C_{th}, it is evident that the majority of AE events are classified as tensile type (Fig. 7 (left)).

The time-dependent changes in *C* (Hz·V/sec) and the proportions of tensile-type AEs and shear-type AEs are shown in Fig. 7 (middle) and Fig. 7 (right). During normal opening and normal closure of rock fractures, which correspond to the sections not colored in Fig. 7 (middle), almost all AE events are classified as tensile type. On the other hand, during the periods when hydraulic shear slips are triggered, a mixture of shear-type AEs become distinct. Based on Fig. 7 (right), the percentages of tensile-type
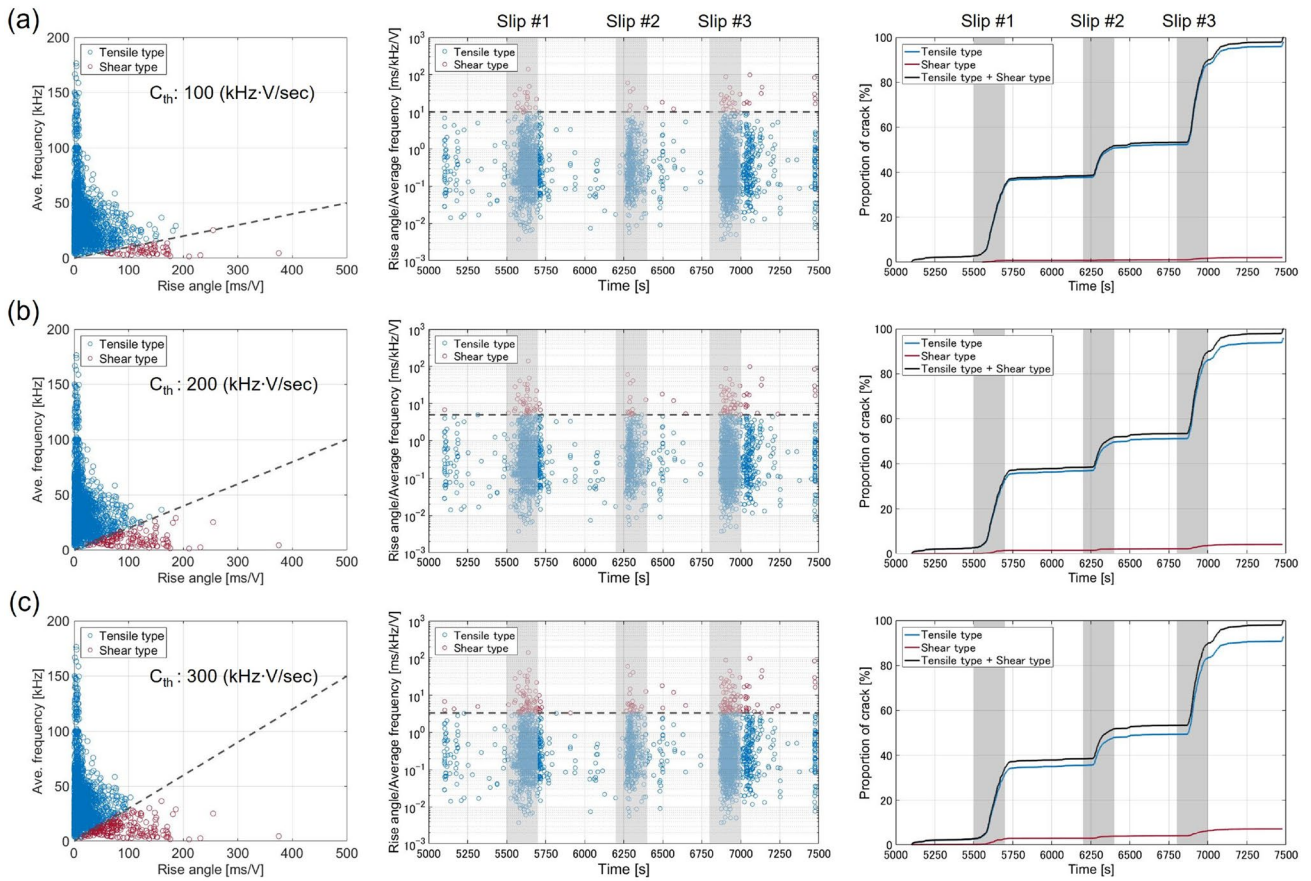
Fig. 7 (Left) Crack mode classification for the entire period of hydraulic shear experiment. (Middle) Time-dependent changes in the ratio of rise angle (RA) to average frequency (AF). The dashed lines indicate the thresholds used to classify tensile and shear types.

(Right) Time-dependent changes in the proportions of tensile-type AEs and shear-type AEs. The threshold classifying tensile and shear types (i.e., C_{th} = RA/AF) is adjusted in three variations: (**a**) 100 kHz·V/sec, (**b**) 200 kHz·V/sec, and (**c**) 300 kHz·V/sec

Table 2 Summary of failure mode classification between tensile and shear types

C_{th} (kHz·V/sec)	After Slip #1 (5740 s)		After Slip #2 (6500 s)		After Slip #3 (7100 s)	
	Tensile (%)	Shear (%)	Tensile (%)	Shear (%)	Tensile (%)	Shear (%)
100	36.4	0.8	51.4	1.1	94.3	1.9
200	35.6	1.6	50.3	2.2	92.2	4.1
300	34.6	2.9	48.6	3.9	89.2	7.0

AEs and shear-type AEs at the completion of each hydraulic shear slip (i.e., 5740, 6500, and 7100 s) are summarized in Table 2. This table allows us to quantitatively reaffirm that the majority of AE events occurring during hydraulic shear slips are classified as tensile type. At the completion of the third hydraulic shear slip, 89–94% AE events are classified as tensile type, whereas 2–7% AE events are classified as shear type. The considerable number of tensile-type AEs are caused by asperity damages under the high effective normal stress of > 50 MPa during shear slip, that contributes to the significantly high ratio of tensile- to shear-type AEs.

Figure. 8 illustrates the temporal changes in Gutenberg–Richter b-values, which are derived for each AE data by two independent AE sensors during the laboratory hydraulic shear experiment. The estimation of b-values for laboratory AEs commonly employs the maximum likelihood method (Utsu 1999), as described earlier. When investigating the time-dependent changes in b-values, there are generally two types of analysis methods. One approach involves utilizing a sliding window that contains a constant number of AE events, while the other approach employs a sliding time window of constant fixed duration. The former analysis necessitates specifying (1) the number of AE events

Fig. 8 Time-dependent changes in the Gutenberg–Richter *b*-values during the hydraulic shear experiment. For estimating the *b*-values, the number of events for analysis is held constant in (**a**, **b**), while the time window length is maintained constant in (**c**, **d**). The specific parameters employed for each analysis method are also provided in the figure
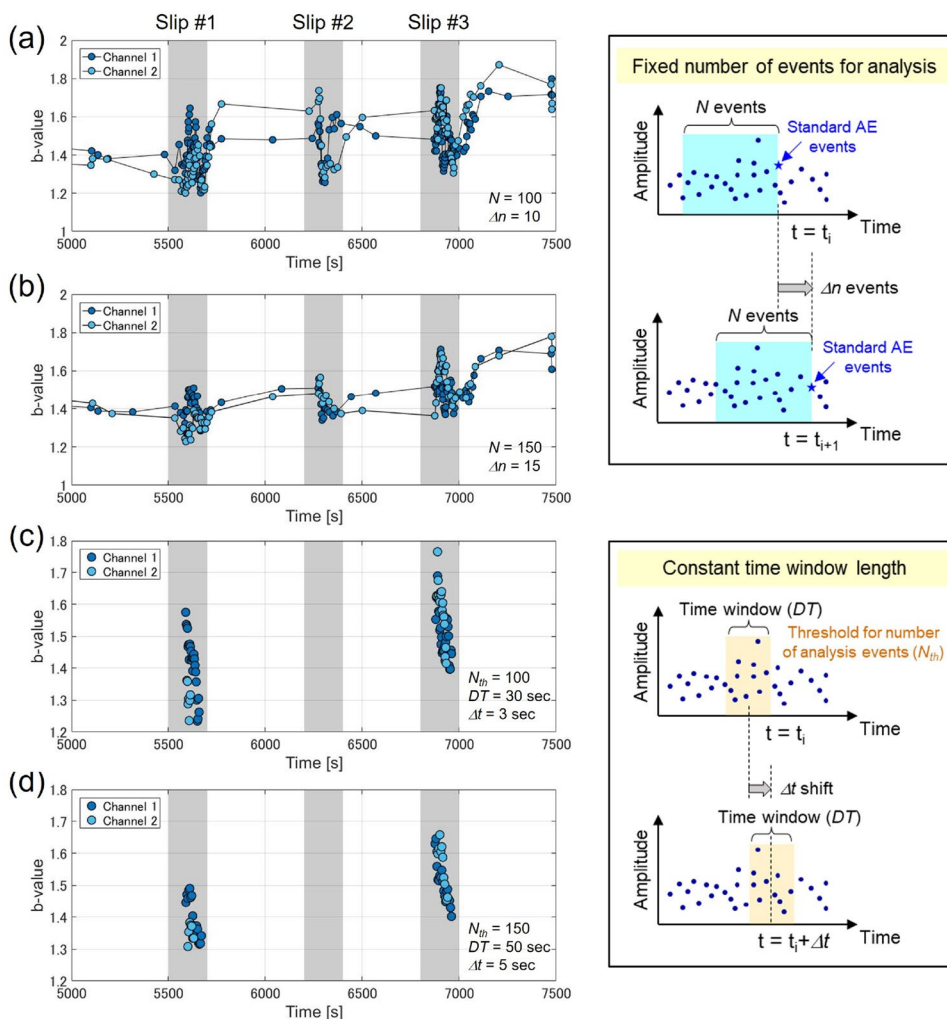
to be analyzed and (2) the number of AE events to skip while sliding the window (Fig. 8 (Top right)). In contrast, the latter analysis requires specifying (1) the duration of the time window, (2) the time interval for sliding the window, and (3) the threshold for the number of AE events to be included in the analysis (Fig. 8 (Bottom right)). Given the absence of definitive criteria for selecting the appropriate *b*-value analysis method, we conducted both types of analysis, varying the parameter sets associated with each, to ensure the consistency of the analysis results. Figure 8a, b exhibits representative results of the time-dependent changes in *b*-values using sliding windows with a constant number of AEs (100 and 150, respectively), while Fig. 8c, d shows the results obtained using a sliding window of fixed duration (30 and 50 s, respectively). Throughout the series of analyses, the patterns of *b*-values increase and decrease generally aligned between the AE data from Channel 1 and Channel 2, and the perturbations in *b*-values diminish as the number of AE events included in the analysis increases. In Fig. 8a, b, discerning clear trends in *b*-value changes during hydraulic

shear slips proves challenging regardless of the chosen parameters. This difficulty arises, because most AE events occur during the timing of each hydraulic shear slip, resulting in a significant disparity in the number of AEs observed between the shear slip periods and other periods, such as normal opening and normal closure of the rock fracture. Conversely, in both Fig. 8c, d, gradual decreases in *b*-value can be observed during the 1st and the 3rd hydraulic shear slips, although the evaluation of *b*-value during the 2nd slip is precluded due to an insufficient number of AE events. Notably, this study cannot capture the *b*-value changes immediately after the start of pressurized water injection, primarily due to the limited number of AE events recorded throughout the entire experimental period. The *b*-values of laboratory AEs range from 1.2 to 1.8 in Fig. 8c and from 1.3 to 1.7 in Fig. 8d, aligning with the ranges observed in previous studies on laboratory-scale experiments (Bolton et al. 2021; Lei et al. 2011; Rivière et al. 2018). Considering the overall agreement in trends between Fig. 8c, d, this study concludes that Fig. 8d is representative of the
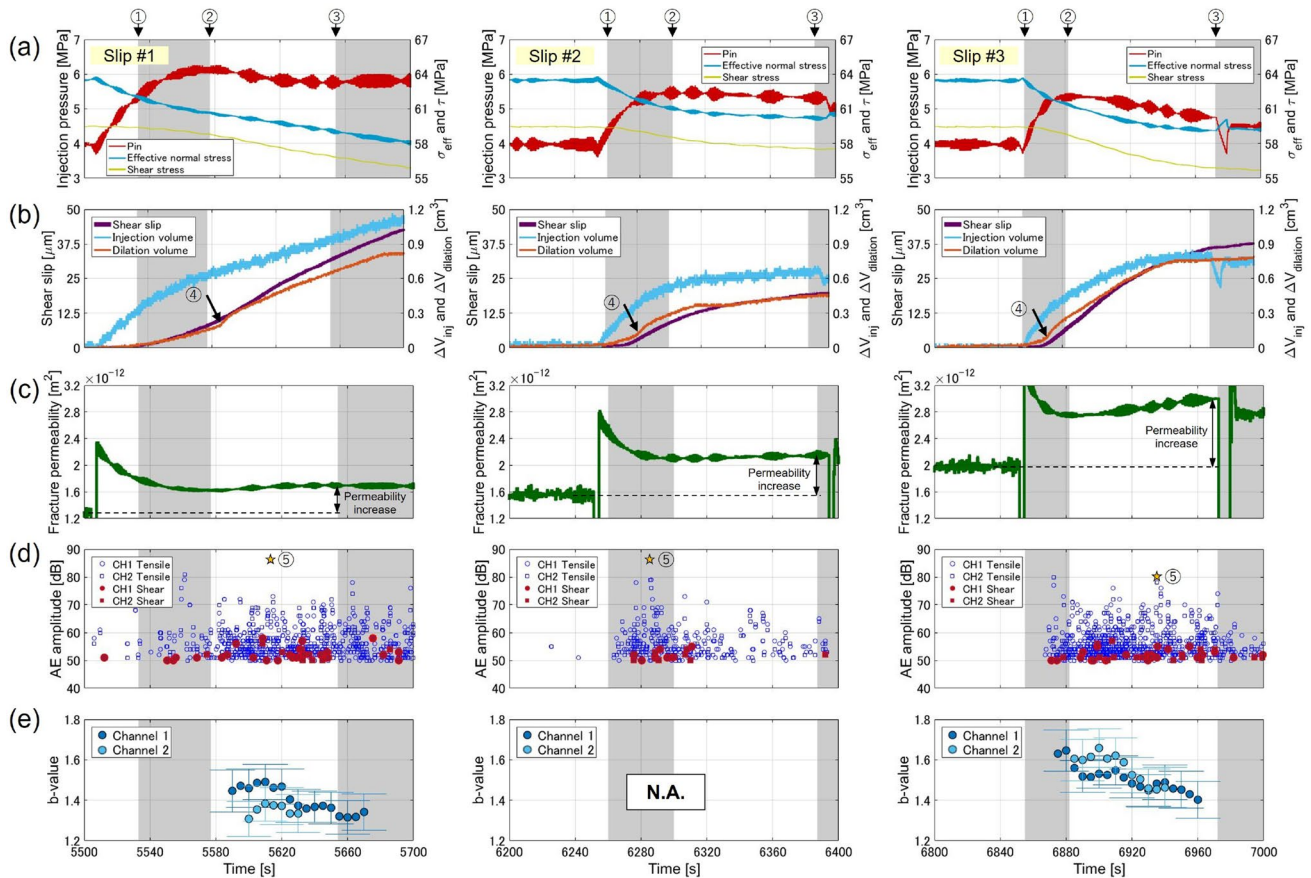
Fig. 9 Detail hydraulic–mechanical–seismic coupled behaviors during hydraulic shearing ((Left) the 1st shear slip, (Middle) the 2nd shear slip, and (Right) the 3rd shear slip in the experiment fr052). Time-dependent changes in (**a**) P_{in}, τ and σ_{eff}, (**b**) shear slip, injection volume, and dilation volume, (**c**) fracture permeability, (**d**) AE amplitude with tensile/shear information, and (**e**) the Gutenberg–Richter *b*-values having estimated errors. Note that ① onset of shear slip, ② time of maximum injection pressure, ③ time of maximum fracture permeability, ④ onset of shear dilation, and ⑤ time of occurrence of the maximum amplitude AE event are marked in these figures

time-dependent changes in *b*-values and serves as the basis for subsequent analyses and discussions.

3.3 Hydraulic–Mechanical–Seismic Coupled Behaviors of Granite Fracture During Hydraulic Shear Slips

The Hydraulic–mechanical–seismic coupled behaviors of granite fractures during hydraulic shear slips (Slip #1, #2, and #3 in Fig. 5) are thoroughly examined in Fig. 9. We present the temporal changes in injection fluid pressure and shear/effective normal stresses on the fracture plane in Fig. 9a, wherein τ and σ_{eff} are calculated using Eqs. (2) and (4), respectively. Furthermore, Fig. 9b illustrates the time-dependent changes of shear slip displacement (d_{slip}), total injection volume (ΔV_{inj}), and fracture dilation volume (ΔV_{dil}), with d_{slip} and ΔV_{inj} calculated using Eqs. (6) and (9), respectively, while ΔV_{dil} corresponds to the change in remaining volumes of syringe pump A (see Fig. 2b).

Figure 9c shows the time-dependent changes in fracture permeability, which are calculated by combining Eqs. (7) and (8). It should be noted that the step-like increase and subsequent gradual decline in fracture permeability are due to switching the control mode of syringe pump B from constant pressure to constant flow rate, and they are not essential changes in fracture permeability (i.e., transient flow regime). Additionally, Fig. 9d shows the time-dependent changes in AE amplitudes and their tensile/shear classifications at a threshold (C_{th}) of 200 (kHz·V/sec), whereas Fig. 9e depicts those in *b*-values of laboratory AEs along with their standard errors, calculated using Eqs. (14) and (15). In Fig. 9, specific positions corresponding to the onset of shear slip (①), time of maximum injection pressure (②), time of maximum fracture permeability (③), onset of shear dilation (④), and time of occurrence of maximum amplitude AE event (marked with orange stars in Fig. 9d, ⑤) are indicated.

During all hydraulic shear slips (Slip #1, #2, and #3), the onset of shear slip consistently precedes the timing of

maximum injection fluid pressure. As the shear slip displacement increases, the slip velocity gradually decelerates and finally stops. The onset of shear dilation follows the time of maximum injection pressure in Slip #1, whereas in Slip #2 and #3, these timings are reversed (Fig. 9a, b). Throughout the periods from the time of maximum injection pressure to the time of maximum fracture permeability, the injection fluid pressure typically decreases, despite the increase in ΔV_{inj}. This result supports the notion that new void/pore spaces are created and sustained during hydraulic shear slips. The dilation volume ($\Delta V_{dilation}$) resulting from both normal opening and shear-induced dilation is consistently constrained by the total injection volume (ΔV_{inj}). With increasing the number of hydraulic shear slip, though the injection flow rate for pressurization increases from 1.5 to 3.0 cm³/min, the maximum injection fluid pressure decreases from 6.3 to 5.5 MPa, implicitly indicating a reduction in contacting asperities and the weakening of the rock fracture. Conversely, the maximum fracture permeability increases from 1.3×10^{-12} to 3.0×10^{-12} m², providing definitive evidence that the concept of "self-propping shear slip" indeed governs the retention of fracture permeability enhancement in granite even under a stress state exceeding ~50 MPa (Fig. 9c).

In Fig. 9b, d, we find that the significant increase in AEs correspond not to the onset of shear slip, but rather to the onset of shear dilation. Notably, the onset of shear dilation is identified by changes in the increasing trend of dilation volume. Figure 9d further reveals that the shear-type AEs are not concentrated within specific periods but are distributed evenly throughout each shear slip. Moreover, laboratory AE events with large amplitudes ($AE_{max\ amp.}$) are not necessarily classified as shear type. $AE_{max\ amp.}$, also classifies as tensile type, are depicted with orange stars in Fig. 9d. While it is common for $AE_{max\ amp.}$ to occur during shear dilation, accurately predicting the timings of their occurrence (i.e., the delay of maximum amplitude AE relative to the onset of shear dilation) remains challenging, even in laboratory-scale phenomenon. The amplitude of $AE_{max\ amp.}$ decreases with increasing number of experienced hydraulic shear slip, and there is no correlation between the amplitude of $AE_{max\ amp.}$ and the incremental amount of fracture permeability. Figure 9e demonstrates that the b-value gradually decreases during shear dilation and the associated permeability increase of the fracture. Upon the completion of shear slip and the restoration of both normal and shear stresses to levels prior to the shear slip, the b-value also returns to a level slightly higher than that at the onset of the preceding shear slip. To the best of our knowledge, our study is the first to reveal the evolution of b-value during hydraulic shear slip of a single granite fracture with surface roughness. In summary, our study suggests that, from a seismological point of view, the most promising indicator potentially correlated with fracture permeability change is the b-value, while the evolution of AE's amplitude and tensile/shear classifications, or the timing of occurrence of $AE_{max\ amp.}$ itself, may not provide useful real-time information for estimating changes in fracture permeability.

4 Discussion

Based on a series of our experimental findings, we delve into the micromechanical phenomenon to explain the changes in fracture permeability and b-value during hydraulic shear slip. Figure 10 (top left) shows the heterogeneous aperture distributions of the rock fracture with a single-point contact before shear slip, determined through high-resolution surface topography analysis of fractures (e.g., vertical resolution of 0.5 μm and horizontal resolution of 23.4 μm). The areas marked in blue correspond to quasi-contacting asperities, whereas the areas marked in colors other than blue correspond to the potentially remaining aperture openings in stressed state. The contacting asperities do not exhibit a uniform structure but are considered to have a hierarchical arrangement (Ishibashi et al. 2015; Vogler et al. 2018), wherein larger contacting asperities are fewer in number (as schematically illustrated in Fig. 10 (top right)). Due to such a heterogeneous aperture distribution, preferential flow paths (e.g., Brown 1989; Ishibashi et al. 2015) spontaneously form within the rock fractures during fluid injection (Fig. 10 (bottom left)). With continued fluid pressurization, the shear failure criteria of Eq. (5) are locally satisfied, and localized shear slips are expected to occur primally around small contacting asperities. This is due to the higher probability of flow paths encountering small contacting asperities compared to large ones. This notion is substantiated by the correlation between event frequency and maximum amplitude of AEs presented in Fig. 6, where AE events characterized by smaller amplitudes approximately correspond to contact asperities of smaller scales, and conversely, larger amplitudes correspond to larger asperities. Once local shear slip occurs, new porosity is generated, contributing to the irreversible increase in fracture permeability (Ishibashi et al. 2023; Ye & Ghassemi 2018). As the areas corresponding to contacting asperities gradually saturate with pressurized fluid, further shear slip is inhibited, resulting in a lower b-value during shear slip (Fig. 10 (bottom right)). Conversely, as shown in Fig. 10 (middle), microfracture propagation from stress concentrations or gouge production within the fracture are inevitable during hydraulic shear slip. These newly generated microstructures play a role in magnifying the b-value when the stress level is restored, and the hydraulic shear slip is triggered again.

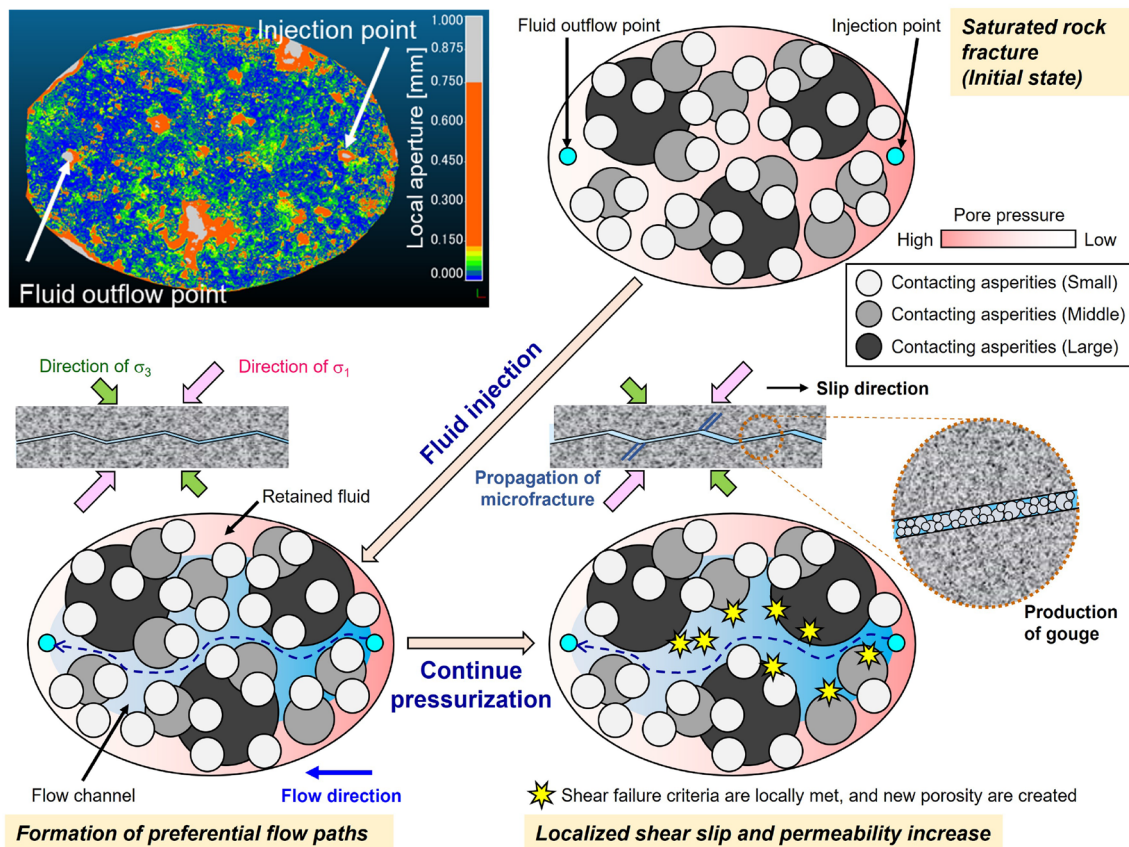Our experimental findings further illustrate two noteworthy observations. Firstly, there is a potential correlation

Fig. 10 Heterogeneous aperture distributions of the rock fracture with a single-point contact before shear slip (top left) and schematic illustration of the micromechanical phenomenon to elucidate the change in the *b*-value during hydraulic shear slip

between changes in fracture permeability and changes in *b*-value during hydraulic shear slip of a single rock fracture at the laboratory scales. Secondly, there appears to be no clear correlation between changes in fracture permeability and the evolution of AE's amplitude or the timing of occurrence of $AE_{max\ amp.}$. Although not explored in this study due to the limited number of AE sensors, it is conceivable to extract spatial information regarding areas where permeability is likely to have increased by determining the hypocenter locations of AEs (Evans et al. 2005; Fu et al. 2021; Norbeck et al. 2018). In particular, *b*-value monitoring offers ease of implementation and can be one of the most useful methods for qualitatively capturing permeability changes in a subsurface single fracture or fracture networks during fluid injection or other human operations, even at intermediate to field scales.

Nevertheless, despite the best possible real-time seismological analyses during fluid injection, it remains challenging to indirectly quantify subsurface permeability change within a single fracture or fracture network, irrespective of

scale. To achieve such indirect quantifications, it is imperative to interpret the spatio-temporal evolution of seismological parameters in combination with the spatio-temporal evolution of other geophysical parameters. Notably, we believe that time-lapse 3D electrical geophysical imaging stands as one of the most powerful tools at present time. For instance, a recent study by Johnson et al. (2021) successfully imaged dilation and closure of subsurface fractures using time-lapse 3D electrical resistivity tomography during high-pressure injection into a dense fractured rock mass at a scale of tens of meters. Therefore, unraveling the hydraulic–mechanical–electrical coupled behaviors of rock fractures can significantly enhance the accuracy of converting electrical properties into hydraulic properties within fractured rock masses. Despite the challenges of measuring 3D electrical properties deep underground and overcoming scale effects in subsurface characterizations, integrating seismological and electrical analyses hold the most promise for achieving indirect estimation of subsurface permeability change within fractured rock masses.

5 Conclusion

In our investigation of geophysical indicators of fracture permeability change, we thoroughly evaluated the hydraulic-mechanical-seismic coupled behaviors of granite fractures with surface roughness during hydraulic shearing under stress states. While we did not determine the hypocenter location of AEs during the experiment in this study, owing to the limited number of AE sensors, our laboratory experiment revealed several important insights: (1) the "self-propping shear slip concept" certainly holds as a prime mechanism for retaining fracture permeability increase of granite, even under stress states exceeding ~ 50 MPa; (2) Gutenberg–Richter b-value gradually decreases during shear dilation and the associated permeability increase of the fracture, making it a potential indicator to investigate fracture permeability changes; and (3) the evolution of AE's amplitude and tensile/shear classification, or the time of occurrence of $AE_{max\ amp.}$ itself, may not be reliable sources of information for estimating fracture permeability change. This decrease in the b-value can be attributed to the spontaneous formation of preferential flow paths during the injection of pressurized fluid into the rock fracture and the subsequent detachment of small contacting asperities due to local shear slips.

While these novel insights have been obtained, it is evident that real-time seismological analysis alone may be insufficient to achieve the indirect quantification of subsurface permeability change in fracture or fracture networks during fluid injection or other human operations. To realize such indirect quantifications of subsurface permeability changes, it is crucial to interpret the spatio-temporal evolution of seismological parameters in combination with the spatio-temporal evolution of other geophysical parameters, such as electrical properties. Thus, interpretations from this combined perspective will be pursued vigorously to gain a precise understanding of subsurface permeability structures.

Declarations

References

Barton N, Choubey V (1977) The shear strength of rock joints in theory and practice. Rock Mech 10(1–2):1–54. https://doi.org/10.1007/BF01261801

Berkowitz B, Bour O, Davy P, Odling N (2000) Scaling of fracture connectivity in geological formations. Geophys Res Lett 27(14):2061–2064. https://doi.org/10.1029/1999GL011241

Bolton DC, Shreedharan S, Rivière J, Marone C (2021) Frequency-magnitude statistics of laboratory foreshocks vary with shear velocity, fault slip rate, and shear stress. J Geophys Res Solid Earth. https://doi.org/10.1029/2021JB022175

Bonnet E, Bour O, Odling NE, Davy P, Main I, Cowie P, Berkowitz B (2001) Scaling of fracture systems in geological media. Rev Geophys 39(3):347–383. https://doi.org/10.1029/1999RG000074

Brown SR (1989) Transport of fluid and electric current through a single fracture. J Geophys Res Solid Earth 94(B7):9429–9438. https://doi.org/10.1029/JB094iB07p09429

Brown SR, Scholz CH (1985) Broad bandwidth study of the topography of natural rock surfaces. J Geophys Res Solid Earth 90(B14):12575–12582. https://doi.org/10.1029/JB090iB14p12575

Cornet FH (2015) Elements of crustal geomechanics. Cambridge University Press

Ellsworth WL (2013) Injection-induced earthquakes. Science 341(6142):1225942. https://doi.org/10.1126/science.1225942

Evans KF, Genter A, Sausse J (2005) Permeability creation and damage due to massive fluid injections into granite at 3.5 km at Soultz 1. Borehole observations: PERMEABILITY CREATION IN GRANITE. J Geophys Res Solid Earth. https://doi.org/10.1029/2004JB003168

Fang Y, Elsworth D, Cladouhos TT (2018) Reservoir permeability mapping using microearthquake data. Geothermics 72:83–100. https://doi.org/10.1016/j.geothermics.2017.10.019

Feng X-T, Young RP, Reyes-Montes JM, Aydan Ö, Ishida T, Liu J-P, Liu H-J (2019) ISRM suggested method for in situ acoustic emission monitoring of the fracturing process in rock masses. Rock Mech Rock Eng 52(5):1395–1414. https://doi.org/10.1007/s00603-019-01774-z

Fu P, Schoenball M, Ajo-Franklin JB, Chai C, Maceira M, Morris JP, Wu H, Knox H, Schwering PC, White MD, Burghardt JA, Strickland CE, Johnson TC, Vermeul VR, Sprinkle P, Roberts B, Ulrich C, Guglielmi Y, Cook PJ (2021) Close observation of hydraulic fracturing at EGS collab experiment 1: fracture trajectory, microseismic interpretations, and the role of natural fractures. J Geophys Res Solid Earth. https://doi.org/10.1029/2020JB020840

Fujii Y, Takemura T, Takahashi M, Lin W, Akaiwa S (2005) The feature of uniaxial tensile fractures in granite and their relation to rock anisotropy. Jour Japan Soc Eng Geol 46(4):227–231. https://doi.org/10.5110/jjseg.46.227

Ge S, Saar MO (2022) Review: induced seismicity during geoenergy development—a hydromechanical perspective. J Geophys Res Solid Earth. https://doi.org/10.1029/2021JB023141

Ishibashi T, Watanabe N, Hirano N, Okamoto A, Tsuchiya N (2015) Beyond-laboratory-scale prediction for channeling flows through subsurface rock fractures with heterogeneous aperture distributions revealed by laboratory evaluation. J Geophys Res Solid Earth 120(1):106–124. https://doi.org/10.1002/2014JB011555

Ishibashi T, Watanabe N, Asanuma H, Tsuchiya N (2016) Linking microearthquakes to fracture permeability change: the role of surface roughness: LINKING MEQS TO PERMEABILITY CHANGE. Geophys Res Lett 43(14):7486–7493. https://doi.org/10.1002/2016GL069478

Ishibashi T, Fang Y, Elsworth D, Watanabe N, Asanuma H (2020) Hydromechanical properties of 3D printed fractures with controlled surface roughness: insights into shear-permeability coupling processes. Int J Rock Mech Min Sci 128:104271. https://doi.org/10.1016/j.ijrmms.2020.104271

Ishibashi T, Asanuma H, Mukuhira Y, Watanabe N (2023) Laboratory hydraulic shearing of granitic fractures with surface roughness under stress states of EGS: permeability changes and energy balance. Int J Rock Mech Min Sci 170:105512. https://doi.org/10.1016/j.ijrmms.2023.105512

Jaeger JC, Cook NGW, Zimmerman R (2007) Fundamentals of rock mechanics (Fourth). Wiley-Blackwell, Hoboken

Johnson TC, Burghardt J, Strickland C, Knox H, Vermeul V, White M, Schwering P, Blankenship D, Kneafsey T (2021) 4D Proxy imaging of fracture dilation and stress shadowing using electrical resistivity tomography during high pressure injections into a dense rock formation. J Geophys Res Solid Earth. https://doi.org/10.1029/2021JB022298

Lei X, Tamagawa T, Tezuka K, Takahashi M (2011) Role of drainage conditions in deformation and fracture of porous rocks under triaxial compression in the laboratory: ROLE OF DRAINAGE CONDITIONS IN FAULTING. Geophys Res Lett. https://doi.org/10.1029/2011GL049888

Lin W, Takahashi M, Sugita N (1995) Change of microcrack widths induced by temperature increase in Inada granite. Jour Japan Soc Eng Geol 36(4):34–38. https://doi.org/10.5110/jjseg.36.300

Lin W, Nakamura T, Takahashi M (2003) Anisotropy of thermal property, ultrasonic wave velocity, strength property and deformability in Inada granite. Jour Japan Soc Eng Geol 44(3):175–187. https://doi.org/10.5110/jjseg.44.175

Matsuki K, Chida Y, Sakaguchi K, Glover PWJ (2006) Size effect on aperture and permeability of a fracture as estimated in large synthetic fractures. Int J Rock Mech Min Sci 43(5):726–755. https://doi.org/10.1016/j.ijrmms.2005.12.001

Meng M, Frash LP, Li W, Welch NJ, Carey JW, Morris J, Neupane G, Ulrich C, Kneafsey T (2022) Hydro-mechanical measurements of sheared crystalline rock fractures with applications for egs collab experiments 1 and 2. J Geophys Res Solid Earth. https://doi.org/10.1029/2021JB023000

Norbeck JH, McClure MW, Horne RN (2018) Field observations at the Fenton Hill enhanced geothermal system test site support mixed-mechanism stimulation. Geothermics 74:135–149. https://doi.org/10.1016/j.geothermics.2018.03.003

Oda M, Katsube T, Takemura T (2002) Microcrack evolution and brittle failure of Inada granite in triaxial compression tests at 140 MPa. J Geophys Res Solid Earth. https://doi.org/10.1029/2001JB000272

Ohno K, Ohtsu M (2010) Crack classification in concrete based on acoustic emission. Constr Build Mater 24(12):2339–2346. https://doi.org/10.1016/j.conbuildmat.2010.05.004

Ohtsu M (1996) Quantitative AE techniques standardized for concrete structures. Mag Concr Res 48(177):321–330. https://doi.org/10.1680/macr.1996.48.177.321

Power WL, Tullis TE, Brown SR, Boitnott GN, Scholz CH (1987) Roughness of natural fault surfaces. Geophys Res Lett 14(1):29–32. https://doi.org/10.1029/GL014i001p00029

Rivière J, Lv Z, Johnson PA, Marone C (2018) Evolution of b-value during the seismic cycle: insights from laboratory experiments on simulated faults. Earth Planet Sci Lett 482:407–413. https://doi.org/10.1016/j.epsl.2017.11.036

Schoenball M, Ajo-Franklin JB, Blankenship D, Chai C, Chakravarty A, Dobson P, Hopp C, Kneafsey T, Knox HA, Maceira M, Robertson MC, Sprinkle P, Strickland C, Templeton D, Schwering PC, Ulrich C, Wood T (2020) Creation of a mixed-mode fracture network at mesoscale through hydraulic fracturing and shear stimulation. J Geophys Res Solid Earth. https://doi.org/10.1029/2020JB019807

Scholz CH (2002) The mechanics of earthquakes and faulting, 2nd edn. Cambridge University Press, Cambridge

Shi Y, Bolt BA (1982) The standard error of the magnitude-frequency b value. Bull Seismol Soc Am 72(5):1677–1687. https://doi.org/10.1785/BSSA0720051677

Takahashi M, Hirata A, Koide H (1990) Effect of confining pressure and pore pressure on permeability of Inada granite. Jour Japan Soc Eng Geol 31(3):105–114. https://doi.org/10.5110/jjseg.31.105

U.S. Department of energy. (2019). GeoVision: Harnessing the heat beneath our feet (p. 212). U.S. Department of energy.

Utsu T (1999) Representation and analysis of the earthquake size distribution: a historical review and some new approaches. Pure Appl Geophys 155(2):509–535. https://doi.org/10.1007/s000240050276

Vogler D, Settgast RR, Annavarapu C, Madonna C, Bayer P, Amann F (2018) Experiments and simulations of fully hydro-mechanically coupled response of rough fractures exposed to high-pressure fluid injection. J Geophys Res Solid Earth 123(2):1186–1200. https://doi.org/10.1002/2017JB015057

Witherspoon PA, Wang JSY, Iwai K, Gale JE (1980) Validity of cubic law for fluid flow in a deformable rock fracture. Water Resour Res 16(6):1016–1024. https://doi.org/10.1029/WR016i006p01016

Ye Z, Ghassemi A (2018) Injection-induced shear slip and permeability enhancement in granite fractures. J Geophys Res Solid Earth 123(10):9009–9032. https://doi.org/10.1029/2018JB016045

Yu X, Vayssade B (1991) Joint profiles and their roughness parameters. Int J Rock Mech Min Sci Geomech Abstr 28(4):333–336. https://doi.org/10.1016/0148-9062(91)90598-G

Zang A, Oye V, Jousset P, Deichmann N, Gritto R, McGarr A, Majer E, Bruhn D (2014) Analysis of induced seismicity in geothermal reservoirs—an overview. Geothermics 52:6–21. https://doi.org/10.1016/j.geothermics.2014.06.005